



**HAL**  
open science

## Serial crystallography captures dynamic control of sequential electron and proton transfer events in a flavoenzyme

Manuel Maestre-Reyna, Cheng-Han Yang, Eriko Nango, Wei-Cheng Huang, Eka Putra Gusti Ngurah Putu, Wen-Jin Wu, Po-Hsun Wang, Sophie Franz-Badur, Martin Saft, Hans-Joachim Emmerich, et al.

### ► To cite this version:

Manuel Maestre-Reyna, Cheng-Han Yang, Eriko Nango, Wei-Cheng Huang, Eka Putra Gusti Ngurah Putu, et al.. Serial crystallography captures dynamic control of sequential electron and proton transfer events in a flavoenzyme. *Nature Chemistry*, 2022, 14 (6), pp.677-685. 10.1038/s41557-022-00922-3 . hal-03716098

**HAL Id: hal-03716098**

**<https://hal.science/hal-03716098v1>**

Submitted on 1 Sep 2022

**HAL** is a multi-disciplinary open access archive for the deposit and dissemination of scientific research documents, whether they are published or not. The documents may come from teaching and research institutions in France or abroad, or from public or private research centers.

L'archive ouverte pluridisciplinaire **HAL**, est destinée au dépôt et à la diffusion de documents scientifiques de niveau recherche, publiés ou non, émanant des établissements d'enseignement et de recherche français ou étrangers, des laboratoires publics ou privés.

1 **Serial crystallography captures dynamic control of sequential electron and proton**  
2 **transfer events in a flavoenzyme**

3

4 Manuel Maestre-Reyna<sup>1</sup>, Cheng-Han Yang<sup>1</sup>, Eriko Nango<sup>2,3</sup>, Wei-Cheng Huang<sup>1</sup>, Eka Putra  
5 Gusti Ngurah Putu<sup>1</sup>, Wen-Jin Wu<sup>1</sup>, Po-Hsun Wang<sup>1</sup>, Sophie Franz-Badur<sup>4</sup>, Martin Saft<sup>4</sup>, Hans-  
6 Joachim Emmerich<sup>4</sup>, Hsiang-Yi Wu<sup>1</sup>, Cheng-Chung Lee<sup>1</sup>, Kai-Fa Huang<sup>1</sup>, Yao-Kai Chang<sup>1</sup>,  
7 Jiahn-Haur Liao<sup>1</sup>, Jui-Hung Weng<sup>1</sup>, Wael Gad<sup>1</sup>, Chiung-Wen Chang<sup>1</sup>, Allan H. Pang<sup>1</sup>,  
8 Michihiro Sugahara<sup>2</sup>, Shigeki Owada<sup>5</sup>, Yuhei Hosokawa<sup>6</sup>, Yasumasa Joti<sup>2,5</sup>, Ayumi  
9 Yamashita<sup>2,3</sup>, Rie Tanaka<sup>2,3</sup>, Tomoyuki Tanaka<sup>2,3</sup>, Luo Fangjia<sup>2,3</sup>, Kensuke Tono<sup>5</sup>, Kai-Cheng  
10 Hsu<sup>7</sup>, Stephan Kiontke<sup>4</sup>, Igor Schapiro<sup>8</sup>, Roberta Spadacini<sup>9</sup>, Antoine Royant<sup>10,11</sup>, Junpei  
11 Yamamoto<sup>6</sup>, So Iwata<sup>2,3</sup>, Lars-Oliver Essen<sup>4,12,\*</sup>, Yoshitaka Bessho<sup>1,2,\*</sup>, Ming-Daw Tsai<sup>1,13,\*</sup>

12 **Affiliations:**

13 <sup>1</sup>Institute of Biological Chemistry, Academia Sinica, 128 Academia Rd. Sec. 2, Nankang,  
14 Taipei, 115, Taiwan.

15 <sup>2</sup>RIKEN SPring-8 Center, 1-1-1 Kouto, Sayo, Hyogo, 679-5148, Japan.

16 <sup>3</sup>Department of Cell Biology, Graduate School of Medicine, Kyoto University, Yoshidakonoe-  
17 cho, Sakyo-ku, Kyoto, 606-8501, Japan.

18 <sup>4</sup>Department of Chemistry, Philipps University Marburg, Hans-Meerwein Strasse 4, Marburg  
19 35032, Germany.

20 <sup>5</sup>Japan Synchrotron Radiation Research Institute, 1-1-1 Kouto, Sayo, Hyogo, 679-5198, Japan.

21 <sup>6</sup>Division of Chemistry, Graduate School of Engineering Science, Osaka University, 1-3  
22 Machikaneyama, Toyonaka, Osaka 560-8531, Japan.

23 <sup>7</sup>Graduate Institute of Cancer Biology and Drug Discovery, College of Medical Science and  
24 Technology, Taipei Medical University, Taipei, Taiwan

25 <sup>8</sup>Fritz Haber Center for Molecular Dynamics, Institute of Chemistry  
26 The Hebrew University of Jerusalem, Jerusalem 91904, Israel

27 <sup>9</sup>Dipartimento di Scienze e tecnologie, Università degli studi del Sannio, Benevento, Italy.

28 <sup>10</sup>Institut de Biologie Structurale (IBS), University Grenoble Alpes, CNRS, CEA, 38044  
29 Grenoble, France.

30 <sup>11</sup>European Synchrotron Radiation Facility, 38043 Grenoble, France.

31 <sup>12</sup>Center of Synthetic Microbiology, Philipps University Marburg, Hans-Meerwein Straße 4,  
32 35032 Marburg, Germany.

33 <sup>13</sup>Institute of Biochemical Sciences, National Taiwan University, 1, Roosevelt Rd. Sec. 4,  
34 Taipei 106, Taiwan.

35

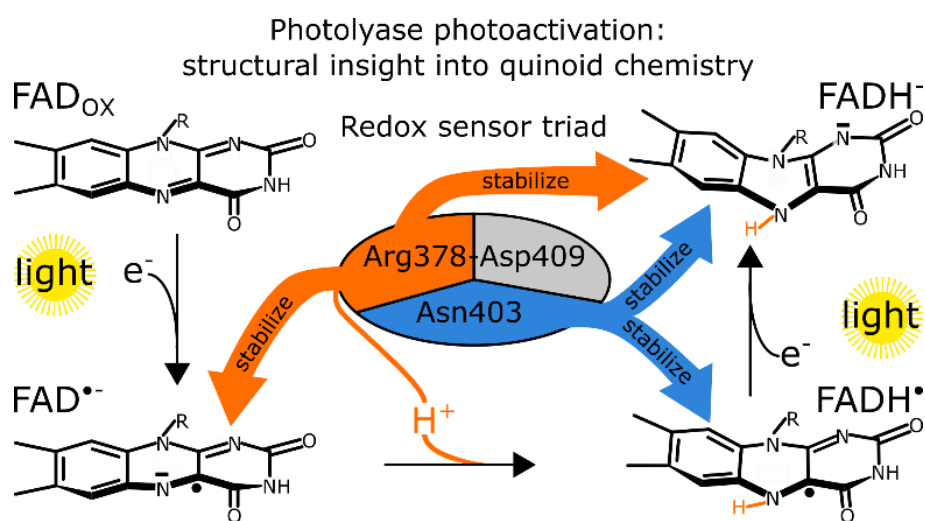
36 **\*e-mail:** mdsai@gate.sinica.edu.tw ; bessho@sinica.edu.tw ; essen@chemie.uni-marburg.de

37

38 **Abstract**

39 **Flavin coenzymes are universally found in biological redox reactions. DNA photolyases**  
40 **with their flavin chromophore (FAD) utilize blue light for DNA repair and**  
41 **photoreduction.** The latter process involves two single-electron transfers to FAD with an  
42 **intermittent protonation step to prime the enzyme active for DNA repair. Here we use**  
43 **time-resolved serial femtosecond X-ray crystallography to describe how light-driven**  
44 **electron transfers trigger subsequent nanosecond-to-microsecond entanglement between**  
45 **FAD and its Asn/Arg-Asp redox sensor triad. We found that this key feature within the**  
46 **photolyase-cryptochrome family regulates FAD re-hybridization and protonation. After**  
47 **first electron transfer, the FAD<sup>•-</sup> isoalloxazine ring *twists strongly* when the arginine**  
48 **closes in to stabilize the negative charge. Subsequent breakage of the arginine-aspartate**  
49 **salt bridge promotes proton transfer from arginine to FAD<sup>•-</sup>. Our molecular movies**  
50 **demonstrate how the protein environment of redox cofactors organizes multiple**  
51 **electron/proton transfer events in an ordered fashion, which could be applicable to other**  
52 **redox systems such as photosynthesis.**

53



54

55

56 All biological systems depend on electron transport chains (ETCs) to fuel their metabolism,  
57 most commonly in the form of photosynthesis and respiration<sup>1,2</sup>. Although ETC proteins, such  
58 as cytochromes and iron-sulphur proteins<sup>3</sup>, can only transfer single electrons, ETC catalyzed  
59 reaction cycles always result in the net flow of two electrons from donor to acceptor<sup>4</sup>. This  
60 apparent paradox is solved by quinoid molecules such as membrane-resident quinones used by  
61 photosynthetic reaction centres and respiratory chains as substrates or enzyme-bound flavin  
62 adenine dinucleotide (FAD) and flavin mononucleotide (FMN) cofactors<sup>5</sup>. These molecules  
63 can capture either one or two electrons and exist hence in three possible redox states: oxidized  
64 (quinone), radical semi-reduced (semiquinone) or fully reduced (hydroquinone)<sup>6</sup>. One  
65 particularly interesting example for multiple electron transfer (ET) reactions on FAD is the  
66 [photoreduction](#) of DNA photolyases, a process by which this ubiquitous class of DNA repair  
67 flavoenzymes reduces their FAD coenzyme to the catalytically active FADH<sup>-</sup> state<sup>7</sup>. Here, two  
68 light-driven, sub-nanosecond, single ET events transform inactive FAD<sub>ox</sub> into the hydroquinoid  
69 FADH<sup>-</sup> via two long-lived radical semiquinone intermediates, FAD<sup>•-</sup> and its subsequently  
70 protonated form FADH<sup>•-</sup> (Fig. 1a)<sup>8</sup>. The ETC fuelling these reactions consists mostly of a  
71 tryptophan triad (Fig 1b)<sup>9,10</sup>, or less frequently a tetrad<sup>11</sup>, which ultimately extracts an electron  
72 from the environment<sup>12</sup>. In the photoactivated state, DNA photolyases finally catalyse blue  
73 light-driven DNA repair of UV photolesions such as cyclobutane pyrimidine dimers (CPD)<sup>13</sup>  
74 (Fig. 1c) by injecting an electron from excited FADH<sup>-\*</sup> onto the DNA lesion and transient  
75 formation of semi-reduced FADH<sup>•-</sup><sup>14</sup>.

76 Over the last three decades, the flavin redox chemistry of photolyases has been extensively  
77 characterized via spectroscopic and theoretical studies at ps-ns (reduction) and μs-ms (re-  
78 oxidation) time-scales<sup>10,12,15-19</sup>. However, information on the stabilization of the post-electron  
79 transfer flavin species (ns-μs) by their surrounding protein matrix, which has been  
80 hypothesized to enable quinoid chemistry<sup>8,20</sup>, is lacking. Furthermore, spectroscopic

81 characterization was mostly restricted to electronic transitions of the flavin species and the ETC,  
82 providing very little information regarding flavin geometry and thereby induced protein  
83 conformational changes<sup>8,10,12,16,21</sup>. In addition, flavin radical intermediates are too short-lived  
84 for conventional crystallographic analysis, and the structures of flavoenzymes often suffer from  
85 radiation-damage due to X-ray mediated flavin reduction<sup>22-25</sup>. Conversely, the recent  
86 development of X-ray free electron laser (XFEL) facilities in combination with serial  
87 femtosecond crystallography (SFX) techniques<sup>26</sup> has allowed for damage-free data collection  
88 of biologically relevant macromolecular structures<sup>27,28</sup>, particularly under time-resolved  
89 conditions (TR-SFX) at ultrashort intervals<sup>22,29-36</sup>.

90 In this study, we structurally characterize FAD redox- and post-electron transfer changes  
91 in the nanosecond to millisecond range, and analyze how each intermediate species is stabilized,  
92 as they occur in the *Methanosarcina mazei* class II DNA photolyase (*MmCPDII*)<sup>23</sup> via TR-  
93 SFX. By analyzing a total of 23 structures, we were able to determine the redox- and time-  
94 dependent structural changes in the FAD coenzyme elicited by the sub-nanosecond  
95 photoreduction events, elucidate the mechanism of FAD<sup>•-</sup> protonation, and uncover an FAD  
96 redox sensor triad Asn/Arg-Asp that differentially stabilizes each flavin redox species, thus  
97 providing unprecedented insight into the structural mechanics of quinoid-protein chemistry.

98

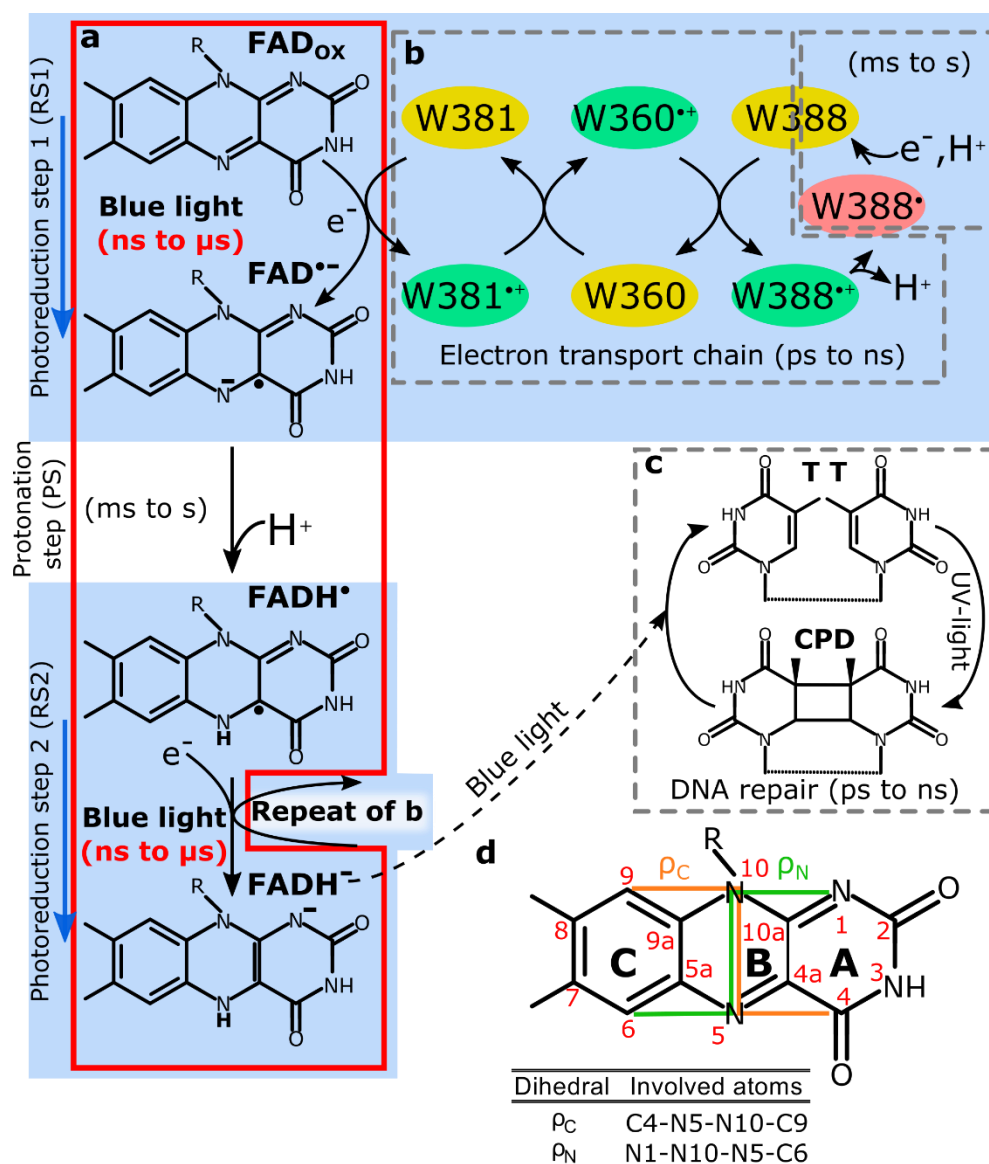


**Figure 1. Reactions catalyzed by DNA photolyases.** (a) During photoactivation, two photoreduction steps (RS1 and RS2, shaded blue) sequentially inject one electron each into FAD, reducing FAD<sub>ox</sub> to FADH<sup>•</sup>. (b) Each photoreduction step involves a tryptophan triad (W381-W360-W388 in *Mm*CPDII), which acts as an electron transport chain. (c) Light-triggered repair of UV-damaged DNA containing a CPD. The time ranges marked in red in (a) were determined in this study, while all other timings are adapted from literature. (d) Isoalloxazine ring structure with definition of dihedral angles  $\rho_C$  (orange) and  $\rho_N$  (green).

## 100 **Results**

101

### 102 **Experimental approach and overall nomenclature**

103 In photolyases, and in the absence of an external reducing agent, photoreduction stalls at the  
104 end of photoreduction step 1 (RS1), unable to proceed to photoreduction step 2 (RS2) without  
105 prior protonation of the anionic semiquinone  $\text{FAD}^{\cdot-}$  to the neutral semiquinone  $\text{FADH}^{\cdot}$ <sup>9,10</sup>. On  
106 the other hand, the neutral semiquinone  $\text{FADH}^{\cdot}$  state is meta-stable at room temperature under  
107 aerobic conditions<sup>22</sup>. Accordingly, static, or steady-state, datasets for the substrates and  
108 products of both electron transfer reactions, i.e. oxidized, neutral semiquinone, and fully  
109 reduced states, could be produced via controlled exposure to light and/or reducing agents  
110 followed by data collection without illumination. Notably the unstable anionic semiquinone  
111 state was an exception, as it could only be obtained via TR-SFX. Meanwhile, the TR-SFX  
112 experiments of the two photoreduction steps could be performed separately, leading to 23  
113 structures (Str1-Str23 in Tables 1 and S1-S3, and Figs. S1 and S2). Each structure is designated  
114 as  $E_{X/Y}$ , with subscript X referring to the initial redox status (ox for oxidized,  $\text{FAD}_{\text{ox}}$ ; semi for  
115 semiquinone,  $\text{FADH}^{\cdot}$ ; and red for reduced,  $\text{FADH}^-$ ), and subscript Y describing their data  
116 collection mode (“ss” for steady state, “dark” for a non-illuminated TR control structure, and  
117 time for the delay after illumination). Furthermore, difference electron density maps<sup>37</sup> were  
118 constructed to highlight structural differences, which are designated as the difference between  
119 two states,  $E_{X'/Y'} - E_{X/Y}$ .

120 To monitor structural changes of the FAD isoalloxazine moiety, we introduce the  $\rho_C$  and  
121  $\rho_N$  dihedral angles (Fig. 1d). These changes happening upon FAD reduction were so far called  
122 butterfly bending and defined as the angle ( $\alpha$ ) between the normal vectors of the A and C ring  
123 planes (Fig. 1d)<sup>38</sup>. Values close to zero degrees were derived for the oxidized flavin state, and  
124 values of 15°-25° for the reduced hydroquinoid state of several flavoproteins<sup>39-41</sup>. However,  $\alpha$

125 cannot discriminate between longitudinal twisting (bending along the long axis crossing the A,  
126 B and C rings) and lateral bending or butterfly-like “buckling” (bending along the short *N5-*  
127 *N10* axis)<sup>38</sup>, whereas  $\rho_C$  and  $\rho_N$  can. When buckling dominates,  $\rho_C \approx \rho_N \approx \alpha$ ; conversely,  $\rho_C \neq \rho_N$   
128 indicates a twist of the isoalloxazine moiety.  
129



131 **Table 1.** Primary properties of the *Mm*CPDII TR-SFX structures.

Str. no.	Str. name	redox state	$\rho_C$ angle	$\rho_N$ angle	distance FADN5-R378N $\epsilon$ (Å) <sup>b</sup>	distance FADN5-N403O $\delta$ (Å) <sup>c</sup>	PDB code	resolution (Å) <sup>d</sup>
0 <sup>a</sup>	E <sub>ox/sync</sub>	FAD <sub>ox</sub>	7.6°	8.7°			7F8T <sup>e</sup>	1.50
1	E <sub>ox/ss</sub>	FAD <sub>ox</sub>	2.0°	2.0°	4.8	3.3	6LT3	2.25
<i>First time-resolved series (FAD<sub>ox</sub> → FAD<sup>•</sup>)</i>								
2	E <sub>ox/dark</sub>	FAD <sub>ox</sub>	2.0°	2.0°	4.8	3.4	6LM4	2.0
3	E <sub>ox/10ns</sub>	FAD <sup>•</sup>	-3.6°	0.8°	4.7	3.6	6LMB	2.55
4	E <sub>ox/50ns</sub>	FAD <sup>•</sup>	3.7°	6.6°	4.6	3.6	6LM5	2.25
5	E <sub>ox/250ns</sub>	FAD <sup>•</sup>	17.1°	11.1°	4.6	3.7	6LM6	2.4
6	E <sub>ox/1<math>\mu</math>s</sub>	FAD <sup>•</sup>	9.5°	13.4°	3.4	4.0	6LM7	2.2
7	E <sub>ox/10<math>\mu</math>s</sub>	FAD <sup>•</sup>	30.9°	14.4°	3.2	3.7	6LM8	2.25
8	E <sub>ox/125<math>\mu</math>s</sub>	FAD <sup>•</sup>	20.3°	18.8°	3.4	4.2	6LMC	3.0
9	E <sub>ox/400<math>\mu</math>s</sub>	FAD <sub>ox</sub> /FAD <sup>•</sup>	5.6°	4.8°	4.5	3.4	6LM9	2.4
10	E <sub>ox/1ms</sub>	FAD <sub>ox</sub>	4.4°	3.1°	4.5	3.4	6LME	3.0
11	E <sub>ox/5ms</sub>	FAD <sub>ox</sub>	3.3°	4.5°	4.8	3.4	6LMA	1.9
<i>Protonation step (FAD<sup>•</sup> → FADH<sup>•</sup>)</i>								
12	E <sub>semi/ss</sub>	FADH <sup>•</sup>	4.6°	4.75°	3.9	2.7	6LT1	2.1
<i>Second time-resolved series (FADH<sup>•</sup> → FADH<sup>•</sup>)</i>								
13	E <sub>semi/dark</sub>	FADH <sup>•</sup>	5.3°	4.7°	3.9	2.7	7CLW	2.10
14	E <sub>semi/10ns</sub>	FADH <sup>•</sup>	9.7°	8.8°	4	2.5	7C3P	2.15
15	E <sub>semi/30ns</sub>	FADH <sup>•</sup>	11.3°	11.5°	3.6	2.7	7C3R	2.1
16	E <sub>semi/100ns</sub>	FADH <sup>•</sup>	11.3°	9.6°	3.7	2.8	7C3W	2.3
17	E <sub>semi/300ns</sub>	FADH <sup>•</sup>	16.5°	16.8°	3.4	2.7	7C3X	2.5
18	E <sub>semi/1<math>\mu</math>s</sub>	FADH <sup>•</sup>	9.7°	9.7°	3.6	2.6	7CLM	2.1
19	E <sub>semi/5<math>\mu</math>s</sub>	FADH <sup>•</sup>	12.7°	11.5°	3.7	2.8	7CLN	2.1
20	E <sub>semi/10<math>\mu</math>s</sub>	FADH <sup>•</sup>	8.5°	8.5°	3.9	2.6	7CLO	2.1
21	E <sub>semi/30<math>\mu</math>s</sub>	FADH <sup>•</sup>	10.9°	10.6°	3.8	2.7	7CLP	2.1
22	E <sub>semi/100<math>\mu</math>s</sub>	FADH <sup>•</sup> /FADH <sup>•</sup>	5.3°	5.5°	3.9	2.6	7CLQ	2.15
<i>Full reduction at steady state</i>								
23	E <sub>red/ss</sub>	FADH <sup>•</sup>	14.3°	14.5°	3.3	3.1	6LT2	2.20

132 <sup>a</sup>Previously reported structure from synchrotron X-ray data<sup>23</sup>. The dihedral angles were not reported,  
133 and were obtained from refining by our procedures.

134 <sup>b</sup>The FADN5-R378N $\epsilon$  distance is between the FAD isoalloxazine N5 atom and the Arg378 N $\epsilon$  atom.

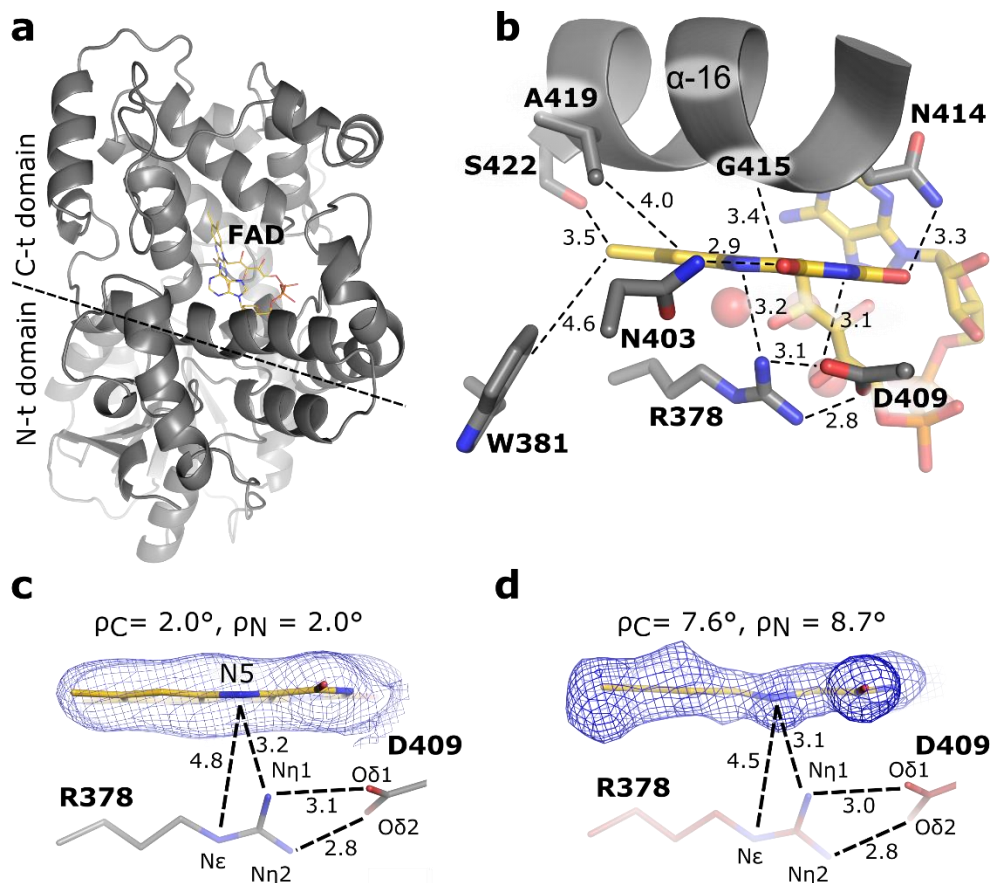
135 <sup>c</sup>The FADN5-N403O $\delta$  distance is between the FAD isoalloxazine N5 atom and the Asn403 O $\delta$ 1 atom.

136 <sup>d</sup>Resolution values given here correspond to the extrapolated structure factor dataset.

137 <sup>e</sup>This structure is derived from 2XRY with dihedral angles refined by the approach of this work.

139 **The damage-free structure of oxidized *Mm*CPDII**

140 Like the structure of  $E_{\text{ox/sync}}$ , previously solved by conventional synchrotron X-ray  
141 crystallography<sup>10</sup> (Str0 in Table 1), our steady-state oxidized structure  $E_{\text{ox/ss}}$  (Str1), solved at  
142 room temperature by SFX, consists of a two-domain topology (Fig. 2a), with the isoalloxazine-  
143 interacting elements being the hydrophobic side of helix  $\alpha 16$  and sidechains of Asn403, Arg378,  
144 and Asp409 (Fig. 2b). However, the isoalloxazine ring of our  $E_{\text{ox/ss}}$  is only slightly buckled  
145 with  $\rho_C$ ,  $\rho_N$  dihedrals of  $2.0^\circ$  and  $2.1^\circ$  (Fig. 2c), substantially smaller than that of  $7.6^\circ$  and  $8.7^\circ$   
146 for the synchrotron structure  $E_{\text{ox/sync}}$  as processed by our approach [for comparison with TR-](#)  
147 [SFX structures](#) (Fig. 2d). The difference can be attributed to  $E_{\text{ox/ss}}$  being the purely oxidized  
148 form as characterized by *in crystallo* UV-Vis [absorption](#) spectra (Fig. S3a), whereas  $E_{\text{ox/sync}}$  has  
149 been partially reduced by synchrotron X-ray irradiation as supported by *in crystallo* spectra<sup>23</sup>.  
150 In addition, as shown in Table 1, the  $E_{\text{ox/dark}}$  structure (Str2, time zero) is nearly identical to the  
151 steady-state  $E_{\text{ox/ss}}$  structure, providing validation for the TR-SFX experiments.



152

**Figure 2. Structure of oxidized *Mm*CPDII photolyase.** (a) Global structure of E<sub>ox/ss</sub> (Str1, steady state oxidized) showing the overall fold with FAD depicted in gold. (b) Isoalloxazine binding pocket with interacting residues (grey sticks) and waters (red spheres). None of the waters are within the hydrogen bonding distance to N5. (c) Geometry of the E<sub>ox/ss</sub> FAD isoalloxazine ring showing minor buckling. (d) Geometry of the isoalloxazine ring from the synchrotron X-ray structure E<sub>ox/sync</sub> (Str0)<sup>23</sup> after reprocessing with our approach, showing increased buckling angles due to radiation-induced photoreduction. In c-d, SigmaA-weighted  $2mF_{\text{obs}} - DF_{\text{calc}}$  omit maps surrounding the isoalloxazine moiety (blue mesh, 1σ contour level) are shown.

153

#### 154 **Changes in active site structures following ET**

155 In both photoreduction steps, structural changes of the isoalloxazine ring and its surrounding  
 156 residues occur after ET, from the first time-point at 10 ns up to roughly 1-10 μs. Detailed  
 157 analyses indicate that these structural changes involve mainly the geometry of the isoalloxazine  
 158 ring, the Arg378-Asp409 salt bridge underneath it, and the sidechain of Asn403 close to the

159 isoalloxazine N5 atom, which are summarized in Table 1. The time courses of the changes in  
160 structural parameters from Table 1 are plotted in Figure 3a,c (RS1) and b,d (RS2), while  
161 representative structures and difference density maps are shown in Figure 3e,h (RS1), g,j (RS2),  
162 and f,i (the protonation step, PS), which will be addressed in subsequent sections.

163 On the other hand, the ETC tryptophans (Fig. 1b) are not a subject of this study as there  
164 are no significant structural changes in either of our time-resolved series (Fig. S4a,b), in  
165 agreement with previous spectroscopic studies indicating that, for *Mm*CPDII, the initial light-  
166 driven electron transfer completes in less than a nanosecond<sup>10</sup>. Interestingly, we did observe  
167 conformational changes of a few residues (H343, H356, and N361) surrounding Trp388 around  
168 the first time-point of 10 ns (Fig. S4c,d), supporting that electron transfer and structural changes  
169 in a redox reaction can be dissected by TR-SFX.

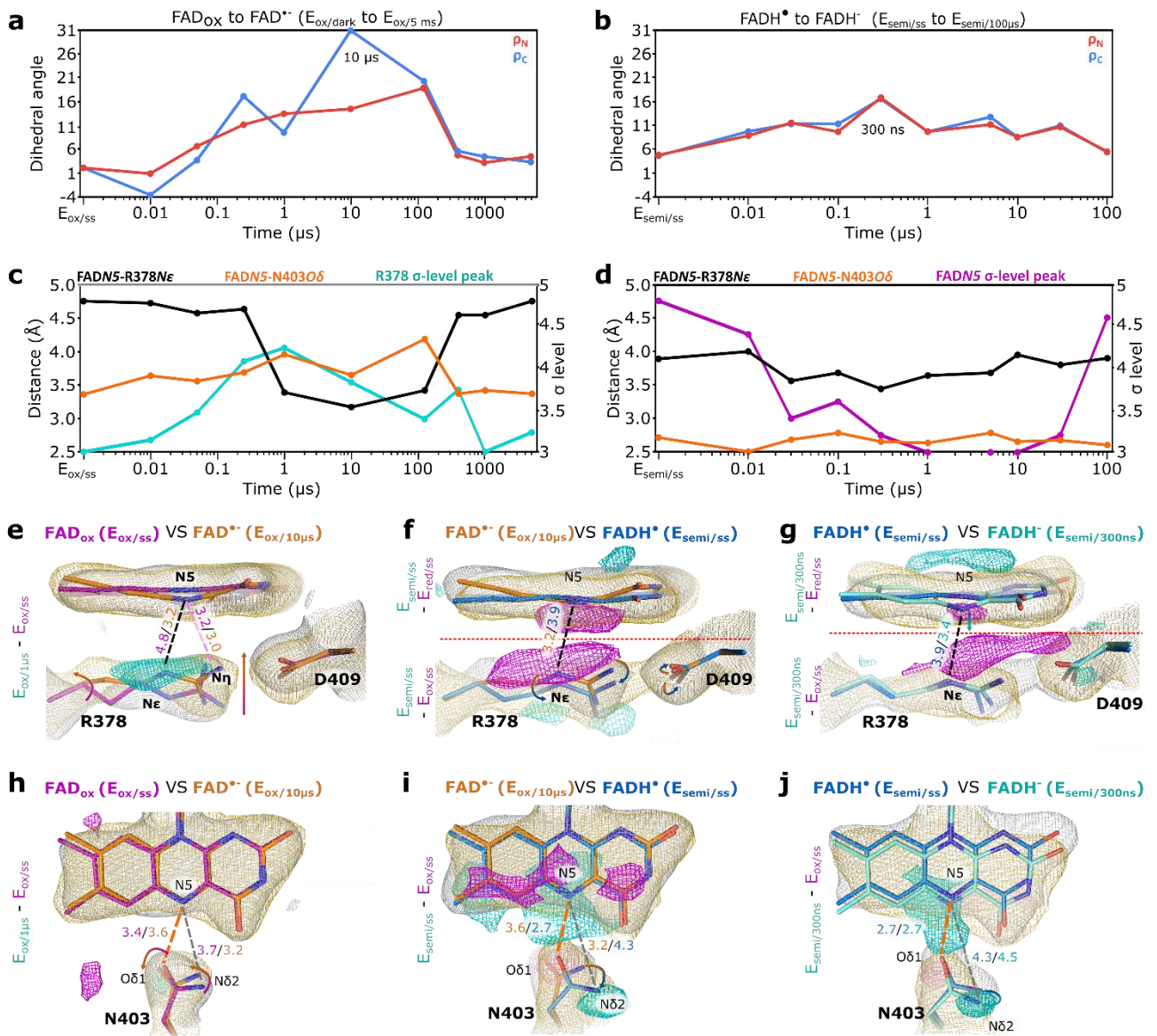
170

### 171 **Changes in the isoalloxazine geometry**

172 During RS1, the FAD<sub>ox</sub> to FAD<sup>•</sup> transition (Fig. 3a),  $\rho_C$  values change from 10 ns, reaching a  
173 maximum at 10  $\mu$ s, whereas  $\rho_N$  values follow the same pattern but with milder changes,  
174 suggesting a twist. On the other hand, from 125  $\mu$ s after photoexcitation,  $\rho_C$  and  $\rho_N$  have both  
175 decreased substantially, and by 400  $\mu$ s have returned to their initial values, correlating well  
176 with the reversion of structural changes in the vicinity Trp388 (Fig. S4c,d). This apparently  
177 reflects FAD<sup>•</sup> reoxidation via back electron transfer toward Trp388<sup>•</sup> (Fig. 1a, b), as under our  
178 experimental conditions the transiently formed tryptophan radical is present due to the lack of  
179 external reductants<sup>9,10</sup>. As indicated by kinetic data<sup>10</sup>, the estimated half-life of FAD<sup>•</sup> is less  
180 than a millisecond (Fig. S3b).

181 During RS2 (FADH<sup>•</sup> to FADH<sup>-</sup>, Fig. 3b), the  $\rho_C$  and  $\rho_N$  dihedral angles increase together  
182 with time and reach a maximum at 300 ns (16.5° and 16.8°, respectively, Table 1), correlating  
183 fairly well with the values in the fully reduced steady-state E<sub>red/ss</sub> (14.3°, 14.5°, respectively).

184 However, they are both reverted to  $\sim 7^\circ$  by 100  $\mu\text{s}$ , again indicating the onset of reoxidation of  
185 the isoalloxazine ring. Accordingly, difference maps relative to  $E_{\text{red/ss}}$  (Fig. 3g and Fig. S2a)  
186 show a negative density peak below the central ring B of the isoalloxazine, which decreases to  
187 the noise level ( $3\sigma$ ) past 300 ns and increases again past 10  $\mu\text{s}$  (Fig. 3d, magenta curve).  
188 Importantly, observation of the parameters reaching a peak and relaxing back in Figure 3a-d  
189 provides further support that the observed small changes are significant and mirror reversible  
190 redox-dependent changes. In summary, the time-resolved structural analysis of both  
191 photoreduction steps illustrates how, after initial ET, the isoalloxazine moiety re-hybridizes to  
192 its new redox state and reaches its final structure in about one **to ten** microseconds. Our results  
193 above expand the description of a redox reaction of FAD to include subsequent structural  
194 changes in addition to the ET steps.



195

196 **Figure 3. Structural changes during the photoactivation of *Mm*CPDII.** (a,b) Evolution of  $\rho_C$  (blue)

197 and  $\rho_N$  (red) dihedral angles over time for photoreductions 1 and 2, respectively. (c,d) Evolution over

198 time of the FADN5-R378Nε (black curve) and FADN5-N403Oδ distances (orange curve), along with

199 plots of the  $\sigma$ -levels of the positive difference peak near R378Nε (c, cyan curve) and the negative

200 difference peak below FADN5 (d, magenta curve). (e-g) Structures of the isoalloxazine ring and the

201 nearby Arg378-Asp409 salt bridge at the beginning and end of each photoreduction step. For RS1 (e),

202 E<sub>ox/ss</sub> (FAD<sub>ox</sub>) is superposed with E<sub>ox/10μs</sub> (FAD<sup>•</sup>), for PS (f), E<sub>ox/10μs</sub> (FAD<sup>•</sup>) with E<sub>semi/ss</sub> (FADH<sup>•</sup>), and

203 for RS2 (g), E<sub>semi/ss</sub> (FADH<sup>•</sup>) with E<sub>semi/300ns</sub> (FADH<sup>-</sup>). Each panel is also superposed with 2 $\sigma$  contoured

204 2DFo-mFc omit maps corresponding to the beginning (grey) and end (gold) states of each

205 photoreduction step, as well as difference maps as indicated by the vertical labels left to the structural

206 moiety. Difference map contour levels: (e) 3 $\sigma$ , (f-g) 3.5 $\sigma$  near the isoalloxazine moiety (above the red

207 dotted line) and 4.0 $\sigma$  near the salt bridge (below the red dotted line). (h-j) Redox- and time-dependent

208 FAD N5-Asn403 interaction for the same structures as in e-g, respectively. Omit maps as above, as well

209 as difference maps relative to  $E_{ox/ss}$  ( $4\sigma$ ) are also shown. In all structures, arrows indicate motion, while  
210 dotted lines the FAD $N5$ -R378 $N\epsilon$  (black) and FAD $N5$ -N403 $O\delta$  (orange) distances in Å. In all difference  
211 density maps, cyan indicates positive and magenta indicates negative.

212

### 213 **Conformational changes of Arg378 concurrent with bending of FAD isoalloxazine ring**

214 For RS1, a positive peak (from difference maps relative to  $E_{ox/ss}$ ) appears above Arg378  $N\epsilon$   
215 (Fig. 3e and Fig. S1a). When its  $\sigma$ -level is plotted against time (cyan curve in Fig. 3c), it reveals  
216 a progressive change peaking at 250 ns to 10  $\mu$ s, followed by a back relaxation till 1-5 ms,  
217 suggesting a movement of Arg378  $N\epsilon$  toward the  $N5$  atom of FAD concurrent with bending  
218 and subsequent relaxation of the isoalloxazine ring. In agreement, the FAD $N5$ -R378 $N\epsilon$   
219 distance (Table 1) decreases and then reverts back following the same pattern (Fig. 3c, black  
220 curve). Importantly, structural analyses indicate that while Arg378  $N\epsilon$  moves toward FAD  $N5$ ,  
221 the bifurcated Arg378-Asp409 salt bridge remains in place (Fig. 3e and Fig. S1a).

222 The same correlation between the FAD $N5$ -R378 $N\epsilon$  distance and isoalloxazine bending  
223 was also observed in RS 2 (FADH<sup>\*</sup> to FADH<sup>-</sup>). As shown by the black curve in Figure 3d, the  
224 distance becomes progressively shorter, reaching a minimum at 300 ns where isoalloxazine  
225 bending is most pronounced (Fig. 3b), and again relaxes back to the starting point at 100  $\mu$ s.  
226 However, the change in the FAD $N5$ -R378 $N\epsilon$  distance in the second set is smaller than that in  
227 the first set (black curves in Fig. 3c,d). Accordingly, the closing between FAD  $N5$  and R378  
228  $N\epsilon$  in the second set is likely caused mainly by the out-of-plane movement of FAD  $N5$ . In  
229 support, the Arg378 sidechain remained unmoved during RS2 as explained below. Meanwhile,  
230 the structural changes and the two different mechanisms described above for the two TR-SFX  
231 series and additional results below can be visualized in Videos S1 and S2.

232

### 233 **Protonation of FAD<sup>-</sup> and weakening of the Arg378-Asp409 salt bridge**

234 Protonation of FAD<sup>•-</sup> at the *N5* position is essential for the photoactivation, as only the neutral  
235 semiquinone FADH<sup>•-</sup> can be further reduced to the active FADH<sup>-</sup> state (Fig. 1a). However, the  
236 proton donor and molecular mechanism remain elusive<sup>42</sup>. Our structural data points toward a  
237 close involvement of the Arg378-Asp409 salt bridge in this step, as its geometry is strongly  
238 affected by the FAD<sup>•-</sup> protonation. As shown in Figure 3f, the Arg378 guanidinium moiety  
239 moves away from the isoalloxazine ring after the FAD<sup>•-</sup> to FADH<sup>•-</sup> conversion, reverting to a  
240 similar position to the oxidized state. However, the geometry of the bifurcated salt bridge is  
241 altered by this FAD<sup>•-</sup> to FADH<sup>•-</sup> conversion, causing Arg378 sidechain to break its salt bridge  
242 with Asp409 with a swivelling motion (Fig. 3f). In support, difference maps from the second  
243 series, relative to E<sub>ox/ss</sub>, reveal a very clear negative signal above the Arg378 sidechain (Fig. 3g  
244 and Fig. S2b), in contrast to the positive difference peaks in the first photoreduction step (Fig.  
245 3e and Fig. S1a). Meanwhile, no significant peaks were observed relative to the fully reduced  
246 state E<sub>red/ss</sub> (Fig. S2a). Furthermore, the intensity of the above mentioned negative difference  
247 map peak remained approximately constant (Fig. S2b), and additional difference map peaks  
248 surrounding guanidinium-carboxylate appeared (Fig. 3f-g).

249 These results, along with absence of other efficient proton donors or water molecules  
250 within hydrogen bonding distance to the isoalloxazine *N5* nitrogen (Fig. 2b), suggest that  
251 Arg378 is likely the proton donor for the protonation of FAD<sup>•-</sup> to FADH<sup>•-</sup>. In support, the  
252 Arg378-Asp409 ionic pair is highly conserved, as database analysis of all known photolyase-  
253 cryptochrome family (PCF) sequences (19524) showed that only three class II photolyases and  
254 six cryptochromes lack this Arg-Asp salt-bridge. Our attempt to construct these unusual natural  
255 mutants resulted in either protein aggregation or loss of FAD binding (Tables S4-S5). Only the  
256 conservative R378K mutation yielded a well-behaved, monodisperse protein capable of FAD  
257 uptake, but at only ~20% stoichiometry (Fig. S5a) and with non-specific binding (Fig. S5b).



258 These results explain why a key function for this highly conserved pair<sup>43-45</sup> has never been  
259 reported before for any member of the PCF.

260

### 261 **Facilitation of protonation and stabilization of the protonated state by Asn403**

262 The *N5* nitrogen of free FADH<sup>•</sup> has been shown to be a weak acid (pK<sub>a</sub> 8.5)<sup>42</sup>, which is  
263 insufficient for its conjugate base FAD<sup>•</sup> to drive proton transfer from Arg378 (pK<sub>a</sub> ~12.5).  
264 However, a previous report showed that the pK<sub>a</sub> of the *N5* nitrogen of flavodoxin's  
265 semiquinone FMNH<sup>•</sup> coenzyme is raised to >13 due to an H-bond with a backbone carbonyl  
266 oxygen<sup>45</sup>. A similar interaction between isoalloxazine *N5* of FADH<sup>•</sup> and the equivalent of  
267 *MmCPDII* Asn403 *OδI* atom has been reported by FT-IR studies of other photolyases<sup>43,44</sup>, a  
268 behavior we can now explain with our structures: In FAD<sub>ox</sub>, Asn403 *OδI* is closer to FAD<sub>ox</sub>  
269 *N5*, while *Nδ2* mainly interacts with the carbonylic FAD<sub>ox</sub> *C4=O*. During RS1, photoreduction  
270 to FAD<sup>•</sup> causes the Asn403 amide sidechain to rotate, with *OδI* moving away from *N5*, while  
271 *Nδ2* approaching it (Fig. 3h). Upon protonation to FADH<sup>•</sup> (Fig. 3i), the Asn403 sidechain  
272 swivels, bringing the Asn403 *OδI* atom in close proximity to the *N5*-H, whereas *Nδ2* moves  
273 to a distal position, which nevertheless allows it to continue interacting with *C4=O* (Fig. S2c).  
274 In accordance with FT-IR data, the FADH<sup>•</sup> state structure (Fig. 3j) is somewhat in-between, as  
275 the Asn403 swivel is partially maintained. Although previous mutagenesis studies of Asn403  
276 in *MmCPDII* suggested an important role in photoreduction<sup>23</sup>, our results provide structural  
277 evidence for stabilization of the protonated state by H-bonding between isoalloxazine *N5* and  
278 Asn403 *OδI*, and support an unusually high pK<sub>a</sub> for the FADH<sup>•</sup> *N5* position in photolyase.

279 Furthermore, the comparison between the FAD isoalloxazine *N5* to Asn403 *OδI* distance  
280 (FAD<sub>N5</sub>-N403*Oδ* distance, orange curves in Fig. 3c-d) and the FAD<sub>N5</sub>-R378*Nε* distance  
281 (black curves in Fig. 3c-d) shows an inverse relationship in both TR sets. Together, the results  
282 suggest that, during RS1, Arg378 approaches the FAD<sup>•</sup> isoalloxazine *N5* but Asn403 *OδI*

283 recedes away. During PS, Arg378 moves away whereas Asn403 *Oδ1* moves in to form an H-  
284 bond with the isoalloxazine *N5*-H. Then, upon RS2, isoalloxazine *N5* moves again toward  
285 Arg378 due to enhanced buckling, leading to slight lengthening of the H-bond with Asn403  
286 *Oδ1*. As shown in Table 1 and Figure S2b, the  $E_{\text{semi}/300\text{ns}}$  structure is strikingly similar to the  
287 steady-state reduced structure  $E_{\text{red/ss}}$ . These results indicate intricate coordination between  
288 Arg378 and Asn403 to mediate the two photoreduction and protonation steps and stabilize the  
289 intermediate species in the process.

290

### 291 **The FAD redox sensor triad and the overall mechanism of photoactivation**

292 Our data shows how Asn403, Arg378 and Asp409 function closely as an “FAD redox sensor  
293 triad” to mediate structural changes of the FAD isoalloxazine, from ns to  $\mu\text{s}$  after the initial  
294 electron transfer in both photoreduction steps and the in-between protonation step. The  
295 structural changes are small (Fig. 4a), but they have been exquisitely dissected by a large  
296 number of TR-SFX structures with continuous changes and intricate coordination involving an  
297 extensive H-bonding network (Fig. 4b). While Figure 3a-d show complete forward reaction  
298 and back relaxation for each photoreduction step separately, here we merge the two forward  
299 reactions and address the overall mechanism in four ways: H-bond analysis to show the  
300 variation of each H-bond in each intermediate structure (Fig. 4c), structural schematics based  
301 on the results of individual steps (Fig. 4d), merging of dihedral angles and interatomic distances  
302 from Figure 3 (Fig. 4e), and visual illustration (Video S3). These analyses together are  
303 explained below.

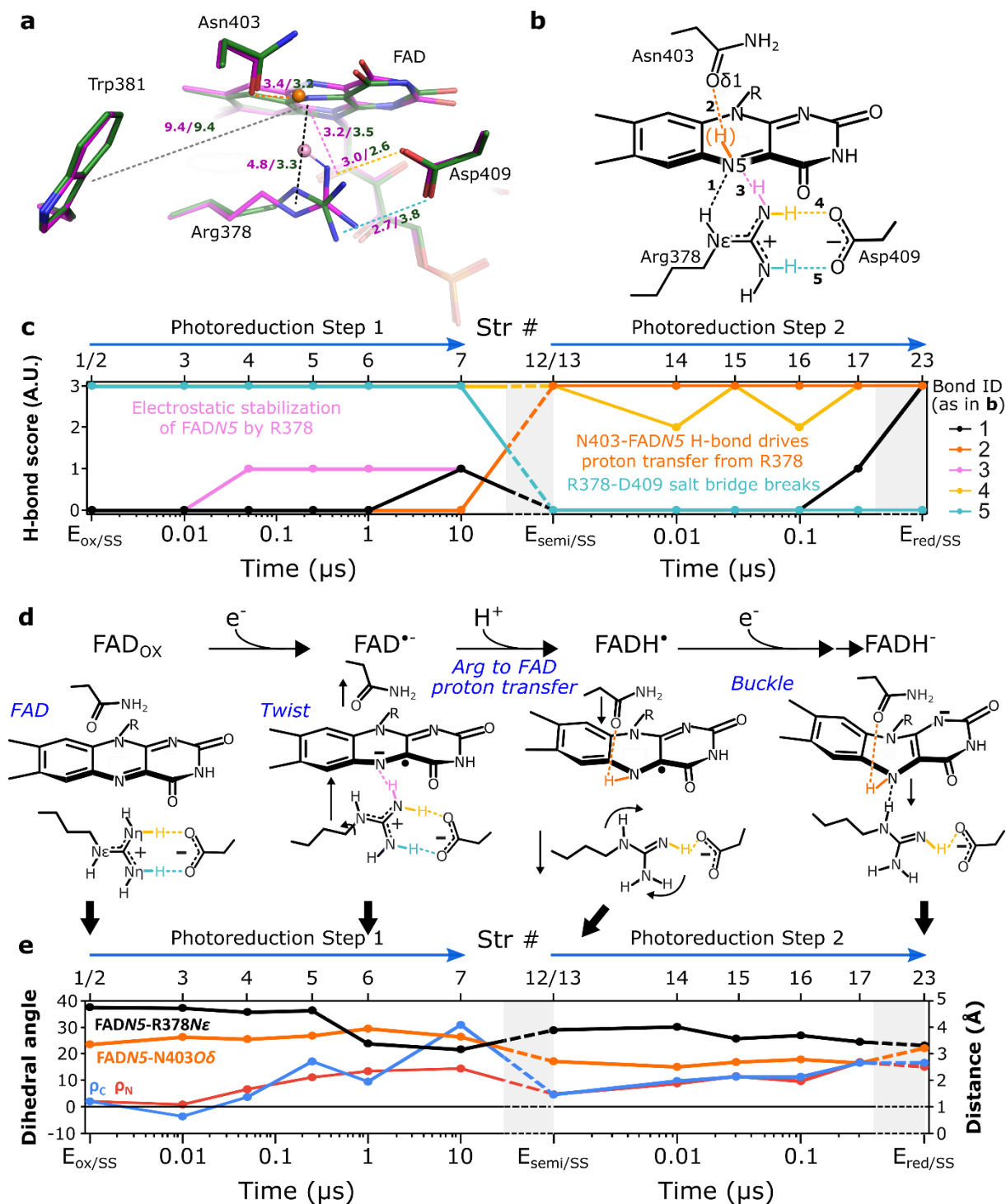
304 In RS1, i.e. the transition from  $\text{FAD}_{\text{ox}}$  to  $\text{FAD}^*$ , a negative charge builds up at FAD *N5*,  
305 electrostatically repulsing the Asn403 *Oδ1* atom and attracting both Asn403 *Nδ2* and, more  
306 importantly, the positive Arg378 sidechain in preparation for protonation. The result is a  
307 transient H-bond between the proximal Arg378 *Nη* and FAD *N5* (Figs. 3e, 4c-d). Accordingly,

308 between 1  $\mu$ s and 125  $\mu$ s (FAD<sup>•-</sup>), the FAD<sub>N5</sub>-R378<sub>N $\epsilon$</sub>  distance is the shortest (i.e. the most  
309 stabilized isoalloxazine moiety), whereas the FAD<sub>N5</sub>-N403<sub>O $\delta$</sub>  distance is the longest (i.e. the  
310 least degree of destabilization) (Figs. 3c, 4e).

311 When the sidechain of Arg378 is close enough to FAD *N5*, proton transfer occurs. FADH<sup>•</sup>  
312 and Arg378, now both neutral, interact only weakly with each other, with Arg378 receding  
313 from the isoalloxazine moiety and the Asp409 sidechain (Fig. 3f). Instead of behaving as an  
314 ionic pair, the Arg378 and Asp409 are now connected by a single H-bond (Fig. 4c-d). A driving  
315 force for the FAD *N5* protonation is its interaction with Asn403 *O $\delta$ I*, which moves in to form  
316 an H-bond, becoming the main stabilizing element for the neutral semiquinone state (Fig. 3i,  
317 E<sub>semi/ss</sub>, FAD<sub>N5</sub>-N403<sub>O $\delta$</sub>  distance 2.7 Å).

318 Then, in RS2, the same trends are observed, with Asn403 *O $\delta$ I* moving slightly away but  
319 still maintaining the hydrogen bond, while isoalloxazine buckling closes the gap to Arg378 *N $\epsilon$* ,  
320 reaching maximal changes at 300 ns to 1  $\mu$ s (Figs. 3d, 3g, 4c-e) and resulting in a very close  
321 approximation of the steady-state E<sub>red/ss</sub>, which represents the fully reduced FADH<sup>-</sup> state, and  
322 where both FAD<sub>N5</sub>-N403<sub>O $\delta$</sub>  and FAD<sub>N5</sub>-R378<sub>N $\epsilon$</sub>  H-bonds contribute to the stabilization of  
323 FADH<sup>-</sup>.

324



325

326 **Figure 4. Mechanistic view of *MmCPDII* photoactivation.** (a) Superposed active site structures of  
 327 *MmCPDII* in the oxidized (purple) and reduced (green) states. The pink ball-and-stick model designates  
 328 the proposed Arg378 proton to be transferred to FAD N5, the orange after transfer. Distances of interest  
 329 are color coded as dashed lines, with the black one corresponding to the FADN5-R378N $\epsilon$  distance,  
 330 while the orange one the FADN5-N403O $\delta$  distance. (b) Schematic representation of key elements in  
 331 the Asn403-isoalloxazine-Arg378-Asp409 H-bonding network. Bonds of interest are labeled by a  
 332 number and a color. (c) Plots summarizing the dynamic behavior of the H-bonding network. Line colors

333 on the graph follow those in (b). H-bond scores are based on a previous PDB-wide analysis and  
334 described in Methods. Briefly, a score of 1 indicates three necessary conditions have been met, while  
335 2, 3 indicate additional favorable conditions. The top axis indicates structure numbers from Table 1. (d)  
336 Structural schematics of the redox and protonation reactions. Only the relevant hydrogen bonds for each  
337 state are shown, color coded as in b and c. (e) Merging of the dihedral angles and distance plots from  
338 Figure 3a-d, showing continuous changes in the entire photoactivation process (i.e., by excluding the  
339 back relaxation time points). In both c and e, a grey background indicates reaction steps whose timing  
340 is not well defined by our experiments.

341

## 342 **Discussion**

343 Overall, this work describes the first structural description of the microscopic processes of the  
344 [photoreduction](#) of a DNA photolyase, highlighting geometric changes of the isoalloxazine  
345 moiety in the re-hybridization process, how they are mediated by Asn403/Arg378-Asp409,  
346 which we name a redox sensor triad, and enable a typical quinone chemistry, namely sequential  
347 pumping of two electrons separated by a protonation step. The X-ray damage-free structure of  
348 *Mm*CPDII shows that the catalytically active FADH<sup>-</sup> chromophore adopts a bending angle of  
349 about 14°, and that bending of the FADH<sup>-</sup> isoalloxazine delicately controls the ET potential by  
350 affecting forward as well as backward electron transfers. Although the observed bending in the  
351 photolyase is well below the degree of bending of FADH<sup>-</sup> in free solution (24°-33°)<sup>46</sup>, it is  
352 significant for the DNA repair mechanism of photolyases as most previous theoretical  
353 calculations on ET reactions between the isoalloxazine and the CPD and (6-4) DNA lesions  
354 predicted planarity of the isoalloxazine due to a lack of interaction with the protein matrix in  
355 QM models<sup>47</sup>. Planarity was also postulated from the photochemistry of catalytically  
356 competent photolyases in the FADH<sup>-</sup> state<sup>8</sup>, because flexible butterfly motions across conical  
357 sections would cause rapid deactivation of excited FADH<sup>-\*</sup> states rather than electron transfer  
358 to the bound DNA lesion. Our structures of the FADH<sup>-</sup> state show that these flexible motions  
359 can be avoided by increased interaction with the arginine and asparagine of the redox triad,

360 thus leading to a higher rigidity of the flavin binding site and explaining the bathochromically  
361 shifted and lifetime-elongated fluorescence emission spectra of FADH<sup>-</sup> in photolyases when  
362 compared to free solution<sup>8</sup>.

363 In terms of the photoreduction to FADH<sup>-</sup>, four features of its molecular mechanism are  
364 fundamental for not only photolyases, but also other flavoenzymes. First, electron uptake in  
365 small molecules in solution and in photolyases by FAD takes place at similar time-scales<sup>9,48</sup>  
366 with subsequent geometric changes requiring only picoseconds in the former<sup>48</sup>. However, we  
367 found that the equivalent response of the protein-embedded isoalloxazine moiety is delayed by  
368 nanoseconds to microseconds. This can now be explained by the role of the protein matrix for  
369 stabilizing otherwise highly unstable intermediates such as FAD<sup>•-</sup> by allowing them to probe a  
370 wide region of the conformational space via twisting and buckling. These transient structural  
371 changes increase the probability of ulterior reactions, first triggering of proton transfer (PT) to  
372 form FADH<sup>•</sup> and then further photoreduction to FADH<sup>-</sup>. This conclusion extends previous  
373 theoretical studies, which proposed that buckling and twisting motions in the isoalloxazine ring  
374 just serve for controlling the redox chemistry of flavins<sup>38</sup>. We found that they can also actively  
375 participate in PT pathways with the embedding protein matrix, thus highlighting the role of the  
376 protein in controlling quinone chemistry.

377 Secondly, our data uncovered a redox sensor triad Asn/Arg-Asp. A structure-based PDB  
378 wide survey in which we searched for flavoproteins presenting an Arg-Asp(Glu) pair nearby  
379 their isoalloxazine moieties returned only PCF members, supporting the unique functional roles  
380 of this conserved motif. Interestingly, within PCF, the third residue, asparagine, is conserved  
381 in enzymatically active photolyases, but not in solely photosensory cryptochromes, where this  
382 residue can be replaced by aspartate like in plant cryptochromes or cysteine in insect  
383 cryptochromes<sup>49</sup>. In those with alternative redox triads (Asp/Arg-Asp and Cys/Arg-Asp), the  
384 quinone chemistry is significantly affected, with photoreduction leading to single electron

385 uptake and protonation to FADH<sup>•</sup> in the former<sup>50</sup>, while the latter arrests photoreduction in the  
386 FAD<sup>•-</sup><sup>51</sup>.

387 Thirdly, despite its high sidechain pKa, the function of arginine as a proton donor has been  
388 suggested for several enzymes<sup>52-56</sup>. Our results provide structural intermediates before and  
389 after protonation of isoalloxazine N5 by Arg378 in the *Mm*CPDII photolyase. Furthermore,  
390 widening the above-mentioned PDB search for non-protein acidic ligands nearby an arginine  
391 and a flavin revealed six flavin-dependent oxidoreductase families (Table S6) with specific  
392 examples from each family shown in Figure S6, including the fumarate reductase mentioned  
393 above<sup>52</sup> and suggesting a potentially wide catalytic role for such an arrangement.

394 Finally, intramolecular ET reactions in photolyases were often understood as simplest  
395 biological model systems for comparable processes during the light-driven charge separation  
396 in photosynthetic reaction centres. The uptake of electrons and protons by quinone substrates  
397 in the Q<sub>B</sub> binding site is known to follow an ordered ET-PT-ET-PT scheme<sup>5</sup>, thus being  
398 comparable to the ET-PT-ET scheme of photolyases, and is accompanied by a redox-dependent  
399 move of Q<sub>B</sub> from a distal to a proximal binding site. Notably, protonation of Q<sub>B</sub><sup>•-</sup> as formed  
400 after first ET is supposed to occur via a serine, Ser-L223 in bacterial reaction centres<sup>57</sup>. Given  
401 our unexpected finding that an arginine conserved in the PCF serves as proton donor to the  
402 flavin cofactor, but not the other candidate asparagine of the redox triad, we expect that similar  
403 time-resolved structural studies will be necessary in future to nail down PT events in other  
404 complex biological redox systems, e.g. the photosynthetic reaction centres.

405

## 406 **Methods**

### 407 **Protein production, crystallization and preparation for XFEL**

408 Protein was produced, and crystals were obtained, by upscaling previously published  
409 conditions<sup>23</sup>. Concentrated crystal slurries were produced by centrifugation of crystallization  
410 batches. For obtaining a fully oxidized dataset, the crystal slurry was then embedded in a  
411 hydrophobic grease matrix in a 1:9 crystal:matrix ratio, as described elsewhere<sup>58</sup>. After this  
412 point, the sample was maintained under far red light (650 nm) at all times to avoid in-situ  
413 photoreduction.

414 For obtaining the semiquinone crystalline material used to acquire the  $E_{\text{semi/ss}}$ ,  $E_{\text{semi/dark}}$   
415 and all  $E_{\text{semi/t}}$  structures (Table 1), the crystal slurry was first supplemented with 50 mM DTT.  
416 For full reduction, the crystal slurry was then exposed to bright white light (Leica KD300) for  
417 5 minutes, and then for partial oxidation to air for another 20 minutes, followed by embedding  
418 in grease matrix. The production and handling of fully photoactivated *Mm*CPDII crystals ( $E_{\text{red/ss}}$ )  
419 was analogous to semiquinone, but to avoid oxidation, the entire procedure was performed  
420 under anaerobic conditions.

421

### 422 **Data collection.**

423 All 23 structures (Str1-Str23 in Tables 1 and S1-S3 and Figs. S1 and S2) were obtained at the  
424 SPring-8 Angstrom Compact free electron LAsER (SACLA)<sup>59</sup>, with crystals being excited via  
425 a nanosecond pulse from a 408 nm OPO laser running at 15 Hz, while data collection from  
426 XFEL pulses at 30Hz.

427

### 428 **Data processing and structural solution**

429 All collected images were initially sorted on-site with cheetah<sup>60</sup>, and then processed off-site  
430 with CrystFEL 0.6.2<sup>61</sup>. Processed datasets were then scaled via SCALEIT, a piece of software  
431 within the CCP4i crystallographic suite<sup>62</sup>. Molecular replacement structural solution was  
432 performed for  $E_{\text{ox/ss}}$  via Phaser, also part of CCP4i, using the [original](#)  $E_{\text{ox/sync}}$ <sup>23</sup> (PDB code  
433 2XRY) as the search model. Further datasets were then solved based on  $E_{\text{ox/ss}}$ , or its derived  
434 structures.

435

### 436 **Overall refinement and structural data visualization**

437 Structure factor extrapolation<sup>31,36,63</sup> was used to refine the subtle time- and redox-dependent  
438 structural changes (Fig. S1 and S2 for the two time-resolved series). Furthermore, difference



439 electron density maps<sup>37</sup> were constructed to highlight these structural differences, which are  
440 designated as the difference between two states,  $E_{X'/Y'}-E_{X/Y}$ . Quantitative analysis of difference  
441 map peaks was normalized to  $\sigma$  levels, i.e. the factor by which a peak's magnitude exceeds the  
442 background electron density. Our results showed that significant difference maps were only  
443 observed in the active site region as shown by examples in Figures S7 and S8. Meanwhile for  
444 RS1, ultrafast conformational changes around 10 ns also occurred in the vicinity of Trp388,  
445 the final electron donor in the electron transfer chain, in the absence of an external reducing  
446 agent (Fig. S4c,d). Since RS2 was performed in the presence of reducing agent DTT, W388•  
447 can be regenerated to W388 and the ultrafast conformational change could not be observed.

448

### 449 **Refinement of the FAD isoalloxazine moiety and its conformational changes**

450 To follow the bending of FAD in our structures, and avoid model bias, the dihedral angles for  
451 all structures, as listed in Table 1, were calculated by adapting previous real space correlation  
452 methods established for the analysis of TR-SFX data as it applies to subtle changes in  
453 photoreceptor chromophores<sup>36,64,65</sup>. Briefly, an equilibrium ensemble for the FAD redox  
454 dependent conformational space was computationally generated based on the  $E_{ox/ss}$ ,  $E_{semi/ss}$  and  
455  $E_{red/ss}$  datasets, from which minimum and maximum  $\rho_C$  and  $\rho_N$  values (Fig. 1d) could be  
456 determined. Then,  $\rho_C$  and  $\rho_N$  restraints within those limits were applied stepwise to each dataset  
457 via three cycles of Phenix refinement<sup>66</sup> using the corresponding resting structure as the initial  
458 model (Fig. S9). The software sfall was then employed to produce calculated structure factors  
459 from both the initial ( $F_{ci}$ ) and refined ( $F_{cref}$ ) models, and  $F_{cref}-F_{ci}$  maps within 2.5 Å of the  
460 isoalloxazine moiety were calculated using the initial model phases, analogously to the  
461 experimental maps presented in e.g. Figure 3. Finally, in order to assess the quality of the  
462 resulting isoalloxazine geometry, the real space correlation coefficient (CC) between the  $F_{cref}-$   
463  $F_{ci}$  and the corresponding  $F_{X'/Y'}-F_{X/Y}$  maps was calculated. Accordingly, we could produce  
464 heat maps where  $\rho_C$  and  $\rho_N$  values were correlated to the CC, to the degree they were able to  
465 reproduce the observed difference density features. A final set of restraints for each individual  
466 structure was then generated as the average and standard deviation of the  $\rho_C$  and  $\rho_N$  with the  
467 top CC score, and all those with at least 95% of that score (Fig. S9). A detailed description of  
468 these and other analysis procedures can be found in Supplementary Methods.

469

### 470 ***In crystallo* UV/Vis absorption spectroscopy**

471 *In crystallo* UV/Vis absorption spectroscopy was performed at the ID29S-Cryobench  
472 Laboratory, ESRF, Grenoble, France<sup>67</sup>. Here, crystals were treated as for the steady-state XFEL  
473 experiments (see above) to photoreduce them into the different redox states. Samples were then  
474 directly mounted on the Cryobench goniometer at 100 K under constant nitrogen gas flow. All  
475 data was acquired with a 25  $\mu\text{m}$  focal point for the probing white light beam, while the detector  
476 optics was connected to the outgoing objective via a 200  $\mu\text{m}$ -diameter optical fiber. Individual  
477 acquisition times were 200 ms, with ten acquisitions being averaged per spectrum.

478

479

## 480 **References**

481

482 1. Belevich, I., Bloch, D. A., Belevich, N., Wikström, M. & Verkhovsky, M. I. Exploring the  
483 proton pump mechanism of cytochrome c oxidase in real time. *Proceedings of the*  
484 *National Academy of Sciences of the United States of America* **104**, 2685–2690 (2007).

485 2. Field, C. B., Behrenfeld, M. J., Randerson, J. T. & Falkowski, P. Primary production of  
486 the biosphere: Integrating terrestrial and oceanic components. *Science* **281**, 237–240  
487 (1998).

488 3. Sun, F. *et al.* Crystal structure of mitochondrial respiratory membrane protein  
489 Complex II. *Cell* **121**, 1043–1057 (2005).

490 4. Alberts, B. *et al.* Electron-Transport Chains and Their Proton Pumps. (2002).

491 5. Nicholls, D. G. & Ferguson, S. J. Respiratory Chains. in *Bioenergetics* 91–157 (Elsevier,  
492 2013). doi:10.1016/b978-0-12-388425-1.00005-1.

493 6. Entsch, B. & Ballou, D. P. Flavins. in *Encyclopedia of Biological Chemistry: Second*  
494 *Edition* 309–313 (Elsevier Inc., 2013). doi:10.1016/B978-0-12-378630-2.00014-1.

495 7. Wang, J., Du, X., Pan, W., Wang, X. & Wu, W. Photoactivation of the  
496 cryptochrome/photolyase superfamily. *Journal of Photochemistry and Photobiology C:*  
497 *Photochemistry Reviews* **22**, 84–102 (2015).

498 8. Kao, Y. T. *et al.* Ultrafast dynamics of flavins in five redox states. *Journal of the*  
499 *American Chemical Society* **130**, 13132–13139 (2008).

500 9. Liu, Z. *et al.* Determining complete electron flow in the cofactor photoreduction of  
501 oxidized photolyase. *Proceedings of the National Academy of Sciences* **110**, 12966–  
502 12971 (2013).

503 10. Müller, P., Ignatz, E., Kiontke, S., Brettel, K. & Essen, L. O. Sub-nanosecond tryptophan  
504 radical deprotonation mediated by a protein-bound water cluster in class II DNA  
505 photolyases. *Chemical Science* **9**, 1200–1212 (2018).

506 11. Nohr, D. *et al.* Extended Electron-Transfer in Animal Cryptochromes Mediated by a  
507 Tetrad of Aromatic Amino Acids. *Biophysical Journal* **111**, 301–311 (2016).

- 508 12. Aubert, C., Vos, M. H., Mathis, P., Eker, A. P. & Brettel, K. Intraprotein radical transfer  
509 during photoactivation of DNA photolyase. *Nature* **405**, 586–590 (2000).
- 510 13. Sancar, A. Mechanisms of DNA Repair by Photolyase and Excision Nuclease (Nobel  
511 Lecture). *Angewandte Chemie - International Edition* **55**, 8502–8527 (2016).
- 512 14. Zhong, D. Electron Transfer Mechanisms of DNA Repair by Photolyase. *Annual Review*  
513 *of Physical Chemistry* **66**, 691–715 (2015).
- 514 15. Zhao, X. *et al.* Reaction mechanism of (6-4) photolyase. *Journal of Biological Chemistry*  
515 **272**, 32580–32590 (1997).
- 516 16. Zhang, M., Wang, L. & Zhong, D. Photolyase: Dynamics and electron-transfer  
517 mechanisms of DNA repair. *Archives of Biochemistry and Biophysics* **632**, 158–174  
518 (2017).
- 519 17. Chaves, I. *et al.* The Cryptochromes: Blue Light Photoreceptors in Plants and Animals.  
520 *Annual Review of Plant Biology* **62**, 335–364 (2011).
- 521 18. Sancar, A. & Zhong, D. It is chemistry but not your grandfather's chemistry.  
522 *Biochemistry* **56**, 1–2 (2017).
- 523 19. Brettel, K. & Byrdin, M. Reaction mechanisms of DNA photolyase. *Current Opinion in*  
524 *Structural Biology* **20**, 693–701 (2010).
- 525 20. Müller, F. Flavin radicals: Chemistry and biochemistry. *Free Radical Biology and*  
526 *Medicine* **3**, 215–230 (1987).
- 527 21. Balland, V., Byrdin, M., Eker, A. P. M., Ahmad, M. & Brettel, K. What Makes the  
528 Difference between a Cryptochrome and DNA Photolyase? A Spectroelectrochemical  
529 Comparison of the Flavin Redox Transitions. *Journal of the American Chemical Society*  
530 **131**, 426–427 (2009).
- 531 22. Park, H., Kim, S., Sancar, A. & Deisenhofer, J. Crystal structure of DNA photolyase from  
532 *Escherichia coli*. *Science* **268**, 1866–1872 (1995).
- 533 23. Kiontke, S. *et al.* Crystal structures of an archaeal class II DNA photolyase and its  
534 complex with UV-damaged duplex DNA. *The EMBO journal* **30**, 4437–49 (2011).
- 535 24. Mees, A. *et al.* Crystal structure of a photolyase bound to a CPD-like DNA lesion after  
536 in situ repair. *Science* **306**, 1789–1793 (2004).
- 537 25. Kort, R., Komori, H., Adachi, S. I., Miki, K. & Eker, A. DNA apophotolyase from *Anacystis*  
538 *nidulans*: 1.8 Å structure, 8-HDF reconstitution and X-ray-induced FAD reduction. *Acta*  
539 *Crystallographica Section D: Biological Crystallography* **60**, 1205–1213 (2004).
- 540 26. Chapman, H. N. *et al.* Femtosecond X-ray protein nanocrystallography. *Nature* **470**,  
541 73–78 (2011).
- 542 27. Neutze, R. & Moffat, K. Time-resolved structural studies at synchrotrons and X-ray free  
543 electron lasers: Opportunities and challenges. *Current Opinion in Structural Biology*  
544 vol. 22 651–659 (2012).
- 545 28. Spence, J. C. H. XFELs for structure and dynamics in biology. *IUCrJ* **4**, 322–339 (2017).

- 546 29. Coquelle, N. *et al.* Chromophore twisting in the excited state of a photoswitchable  
547 fluorescent protein captured by time-resolved serial femtosecond crystallography.  
548 *Nature Chemistry* **10**, 31–37 (2018).
- 549 30. Nango, E. *et al.* A three-dimensional movie of structural changes in bacteriorhodopsin.  
550 *Science* **354**, 1552–1557 (2016).
- 551 31. Nogly, P. *et al.* Retinal isomerization in bacteriorhodopsin captured by a femtosecond  
552 x-ray laser. *Science* **361**, (2018).
- 553 32. Tenboer, J. *et al.* Time-resolved serial crystallography captures high-resolution  
554 intermediates of photoactive yellow protein. *Science* **346**, 1242–1246 (2014).
- 555 33. Skopintsev, P. *et al.* Femtosecond-to-millisecond structural changes in a light-driven  
556 sodium pump. *Nature* **583**, 314–318 (2020).
- 557 34. Kupitz, C. *et al.* Serial time-resolved crystallography of photosystem II using a  
558 femtosecond X-ray laser. *Nature* **513**, 261–265 (2014).
- 559 35. Pande, K. *et al.* Femtosecond structural dynamics drives the trans/cis isomerization in  
560 photoactive yellow protein. *Science (New York, N.Y.)* **352**, 725–9 (2016).
- 561 36. Schmidt, M. Time-resolved macromolecular crystallography at pulsed X-ray sources.  
562 *International Journal of Molecular Sciences* vol. 20 1401 (2019).
- 563 37. Rould, M. A. & Carter, C. W. Isomorphous Difference Methods. *Methods in*  
564 *Enzymology* **374**, 145–163 (2003).
- 565 38. Nakai, S., Yoneda, F. & Yamabe, T. Theoretical study on the lowest-frequency mode of  
566 the flavin ring. *Theoretical Chemistry Accounts* **103**, 109–116 (1999).
- 567 39. Fox, K. M. & Karplus, P. A. Old yellow enzyme at 2 Å resolution: overall structure,  
568 ligand binding, and comparison with related flavoproteins. *Structure (London,*  
569 *England : 1993)* **2**, 1089–105 (1994).
- 570 40. Lennon, B. W., Williams, C. H. & Ludwig, M. L. Crystal structure of reduced thioredoxin  
571 reductase from *Escherichia coli*: Structural flexibility in the isoalloxazine ring of the  
572 flavin adenine dinucleotide cofactor. *Protein Science* **8**, 2366–2379 (2008).
- 573 41. White, T. A., Johnson, W. H., Whitman, C. P. & Tanner, J. J. Structural basis for the  
574 inactivation of *Thermus thermophilus* proline dehydrogenase by N-propargylglycine.  
575 *Biochemistry* **47**, 5573–5580 (2008).
- 576 42. Draper, R. D. & Ingraham, L. L. A potentiometric study of the flavin semiquinone  
577 equilibrium. *Archives of Biochemistry and Biophysics* **125**, 802–808 (1968).
- 578 43. Wijaya, I. M. M., Domratheva, T., Iwata, T., Getzoff, E. D. & Kandori, H. Single  
579 Hydrogen Bond Donation from Flavin N5 to Proximal Asparagine Ensures FAD  
580 Reduction in DNA Photolyase. *Journal of the American Chemical Society* **138**, 4368–  
581 4376 (2016).
- 582 44. Iwata, T., Zhang, Y., Hitomi, K., Getzoff, E. D. & Kandori, H. Key dynamics of conserved  
583 asparagine in a cryptochrome/photolyase family protein by Fourier transform infrared  
584 spectroscopy. *Biochemistry* **49**, 8882–8891 (2010).

- 585 45. Ludwig, M. L., Schopfer, L. M., Metzger, A. L., Patridge, K. A. & Massey, V. Structure  
586 and Oxidation-Reduction Behavior of 1-Deaza-FMN Flavodoxins: Modulation of Redox  
587 Potentials in Flavodoxins. *Biochemistry* **29**, 10364–10375 (1990).
- 588 46. Walsh, J. D. & Miller, A. F. Flavin reduction potential tuning by substitution and  
589 bending. *Journal of Molecular Structure: THEOCHEM* **623**, 185–195 (2003).
- 590 47. Domratcheva, T. Neutral histidine and photoinduced electron transfer in DNA  
591 photolyases. *Journal of the American Chemical Society* **133**, 18172–18182 (2011).
- 592 48. Dereka, B. *et al.* Direct Observation of a Photochemical Alkyne-Allene Reaction and of  
593 a Twisted and Rehybridized Intramolecular Charge-Transfer State in a Donor-Acceptor  
594 Dyad. *Journal of the American Chemical Society* **139**, 16885–16893 (2017).
- 595 49. Kao, Y.-T. *et al.* Ultrafast Dynamics and Anionic Active States of the Flavin Cofactor in  
596 Cryptochrome and Photolyase. *Journal of the American Chemical Society* **130**, 7695–  
597 7701 (2008).
- 598 50. Damiani, M. J., Nostedt, J. J. & O'Neill, M. A. Impact of the N5-proximal Asn on the  
599 thermodynamic and kinetic stability of the semiquinone radical in photolyase. *The*  
600 *Journal of biological chemistry* **286**, 4382–91 (2011).
- 601 51. Berndt, A. *et al.* A novel photoreaction mechanism for the circadian blue light  
602 photoreceptor Drosophila cryptochrome. *Journal of Biological Chemistry* **282**, 13011–  
603 13021 (2007).
- 604 52. Mowat, C. G. *et al.* Kinetic and crystallographic analysis of the key active site acid base  
605 arginine in a soluble fumarate reductase. *Biochemistry* **40**, 12292–12298 (2001).
- 606 53. Senger, M. *et al.* How FeFe-Hydrogenase Facilitates Bidirectional Proton Transfer.  
607 *Journal of the American Chemical Society* **141**, 17394–17403 (2019).
- 608 54. Stevens, D. R. & Hammes-Schiffer, S. Examining the Mechanism of Phosphite  
609 Dehydrogenase with Quantum Mechanical/Molecular Mechanical Free Energy  
610 Simulations. *Biochemistry* **59**, 943–954 (2020).
- 611 55. van der Kamp, M. W., Perruccio, F. & Mulholland, A. J. High-level QM/MM modelling  
612 predicts an arginine as the acid in the condensation reaction catalysed by citrate  
613 synthase. *Chemical Communications* 1874–1876 (2008) doi:10.1039/b800496j.
- 614 56. Keenholz, R. A. *et al.* Arginine as a general acid catalyst in serine recombinase-  
615 mediated DNA cleavage. *Journal of Biological Chemistry* **288**, 29206–29214 (2013).
- 616 57. Paddock, M. L. *et al.* ENDOR spectroscopy reveals light induced movement of the H-  
617 bond from Ser-L223 upon forming the semiquinone (QB-•) in reaction centers from  
618 Rhodospirillum rubrum. *Biochemistry* **46**, 8234–8243 (2007).
- 619 58. Sugahara, M. *et al.* Grease matrix as a versatile carrier of proteins for serial  
620 crystallography. *Nature Methods* **12**, 61–63 (2014).
- 621 59. Yabashi, M., Tanaka, H. & Ishikawa, T. free-electron lasers Overview of the SACLA  
622 facility. *J. Synchrotron Rad* **22**, 477–484 (2015).

- 623 60. Nakane, T. *et al.* Data processing pipeline for serial femtosecond crystallography at  
624 SACLA. *Journal of Applied Crystallography* **49**, 1035–1041 (2016).
- 625 61. White, T. A. *et al.* CrystFEL : a software suite for snapshot serial crystallography.  
626 *Journal of Applied Crystallography* **45**, 335–341 (2012).
- 627 62. Winn, M. D. *et al.* Overview of the CCP4 suite and current developments. *Acta*  
628 *crystallographica. Section D, Biological crystallography* **67**, 235–42 (2011).
- 629 63. Genick, U. K. *et al.* Structure of a Protein Photocycle Intermediate by Millisecond  
630 Time-Resolved Crystallography. *Science* **275**, 1471–1475 (1997).
- 631 64. Carrillo, M. *et al.* High-resolution Crystal Structures of Transient Intermediates in the  
632 Phytochrome Photocycle. *Structure* 2020.09.16.298463 (2021)  
633 doi:10.1101/2020.09.16.298463.
- 634 65. Claesson, E. *et al.* The primary structural photoresponse of phytochrome proteins  
635 captured by a femtosecond x-ray laser. *eLife* **9**, (2020).
- 636 66. Afonine, P. v. *et al.* Towards automated crystallographic structure refinement with  
637 *phenix.refine*. *Acta Crystallographica Section D Biological Crystallography* **68**, 352–367  
638 (2012).
- 639 67. von Stetten, D. *et al.* *In crystallo* optical spectroscopy ( *ic* OS) as a complementary tool  
640 on the macromolecular crystallography beamlines of the ESRF. *Acta Crystallographica*  
641 *Section D Biological Crystallography* **71**, 15–26 (2015).

642

## 643 **Acknowledgments**

644 The XFEL experiments were performed at the BL2 of SACLA with the approval of the Japan  
645 Synchrotron Radiation Research Institute (JASRI) (Proposal No. 2017A8019, 2017B8052,  
646 2018A8008, 2018B8031, 2019A8014, 2019B8005). We would like to thank Tzu-Chun Hsiao,  
647 and Miu-lun Wu for their assistance in sample preparation. We are also grateful to Tomoyuki  
648 Tanaka, Toshi Arima, Yoshinori Matsuura, Hisashi Naitow, Naoki Kunishima, Tetsukon Kin,  
649 and the members of Engineering Support Team of SACLA for help during our X-ray  
650 experiments, as well as to Takanori Nakane for his introduction to CrystFEL. We thank all staff  
651 members of the TPS05A beamline, NSRRC, a national user facility supported by MOST, ROC,  
652 and in particular Chien-Chang Tseng and Chung-Kuang Chou for their help in setting up non-  
653 standard conditions for crystal testing. Also, Hui-Lin Shr (Crystallization Facility of the  
654 Institute of Biological Chemistry, Academia Sinica) provided the location for crystallization  
655 under non-standard conditions, which were initially tested with equipment kindly provided by  
656 Dr. Shin-Guang Shyu. We would like to thank Dr. Thomas C. Terwilliger (Los Alamos  
657 National Laboratory) for his kind help in understanding the theoretical underpinnings of  
658 Bayesian difference refinement. We would also like to thank Guillaume Gottthard for his

659 assistance in acquiring the redox-dependent *in crystallo* spectra at the ID29S-Cryobench  
660 laboratory, which is a platform of the Grenoble Instruct-ERIC center (ISBG; UMS 3518  
661 CNRS-CEA-UGA-EMBL) within the Grenoble Partnership for Structural Biology (PSB).  
662 Finally, we would like to thank Mr. Alvaro Maestre Reyna for help in setting up the necessary  
663 scripts and macros for calculating extrapolated structure factors.

664

### 665 **Funding**

666 The work was supported by Academia Sinica and the Taiwan Protein Project funded by MOST  
667 (Grant No. AS-KPQ-105-TPP and AS-KPQ-109-TPP2), and in part by JSPS KAKENHI  
668 (16K01942). L.O.E. thanks for support by Air Force Office of Scientific Research (AFOSR;  
669 Grant No. FA9550-14-1-0409) and German Research Foundation (DFG, Grant No. ES152/18).  
670 S.I. acknowledges support by Platform Project for Supporting Drug Discovery and Life  
671 Science Research (Basis for Supporting Innovative Drug Discovery and Life Science Research  
672 (BINDS)) from Japan Agency for Medical Research and Development (AMED).

673

### 674 **Author contributions**

675 MMR, SI, LOE, YB, and MDT conceived the research and designed experiments. MMR, CHY,  
676 EN, WCH, EPGNP, WJW, PHW, SFB, MS, HJE, HYW, CCL, KFH, YKC, JHL, JHW, WG,  
677 CWC, AHP, MS, SO, YH, AY, RT, TT, LF, KT, RS, AR, JY, LOE, and YB performed  
678 experiments. MMR, CHY, EN, YJ, SK, IS, LOE, YB, and MDT analyzed the data. MMR,  
679 EPGNP, LOE, and AR performed *in-crystallo* spectroscopy. MMR and CHY established and  
680 analyzed the multiple refinement approach protocol. KCH performed structure-based PDB  
681 search. MMR, WJW, CHY, [AR](#), LOE, YB, and MDT wrote the manuscript.

682

### 683 **Additional information**

684 Supplementary information is available in the online version of the paper. Correspondence and  
685 requests for materials should be addressed to Ming-Daw Tsai. Structural models, along with  
686 structure factors presented here can be found under PDB accession codes [7F8T](#), [6LT3](#), [6LT1](#),  
687 [6LT2](#), [6LM4](#), [6LMB](#), [6LM5](#), [6LM6](#), [6LM7](#), [6LM8](#), [6LMC](#), [6LM9](#), [6LME](#), [6LMA](#), [7CLW](#),  
688 [7C3P](#), [7C3R](#), [7C3W](#), [7C3X](#), [7CLM](#), [7CLN](#), [7CLO](#), [7CLP](#), and [7CLQ](#).

689

### 690 **Competing financial interests**

691 The authors declare no conflict of financial interest.